Estimating repetitive spatiotemporal patterns from many subjects' resting-state fMRIs

Yusuke Takeda [a,b,*], Takashi Itahashi [c], Masa-aki Sato [b], Okito Yamashita [a,b]

[a] Computational Brain Dynamics Team, RIKEN Center for Advanced Intelligence Project, 2-2-2 Hikaridai, Seika-cho, Soraku-gun, Kyoto, 619-0288, Japan
[b] Department of Computational Brain Imaging, ATR Neural Information Analysis Laboratories, 2-2-2 Hikaridai, Seika-cho, Soraku-gun, Kyoto, 619-0288, Japan
[c] Medical Institute of Developmental Disabilities Research, Showa University, 6-11-11 Kita-karasuyama, Setagaya-ku, Tokyo, 157-8577, Japan

ARTICLE INFO

ABSTRACT

Recently, we proposed a method to estimate repetitive spatiotemporal patterns from resting-state brain activity data (SpatioTemporal Pattern estimation, STeP) (Takeda et al., 2016). From such resting-state data as functional MRI (fMRI), STeP can estimate several spatiotemporal patterns and their onsets even if they are overlapping. Nowadays, a growing number of resting-state data are publicly available from such databases as the Autism Brain Imaging Data Exchange (ABIDE), which promote a better understanding of resting-state brain activities. In this study, we extend STeP to make it applicable to such big databases, thus proposing the method we call BigSTeP. From many subjects' resting-state data, BigSTeP estimates spatiotemporal patterns that are common across subjects (common spatiotemporal patterns) as well as the corresponding spatiotemporal patterns in each subject (subject-specific spatiotemporal patterns). After verifying the performance of BigSTeP by simulation tests, we applied it to over 1,000 subjects' resting-state fMRIs (rsfMRIs) obtained from ABIDE I. This revealed two common spatiotemporal patterns and the corresponding subject-specific spatiotemporal patterns. The common spatio-temporal patterns included spatial patterns resembling the default mode (DMN), sensorimotor, auditory, and visual networks, suggesting that these networks are time-locked with each other. We compared the subject-specific spatiotemporal patterns between autism spectrum disorder (ASD) and typically developed (TD) groups. As a result, significant differences were concentrated at a specific time in a pattern, when the DMN exhibited large positive activity. This suggests that the differences are context-dependent, that is, the differences in fMRI activities between ASDs and TDs do not always occur during the resting state but tend to occur when the DMN exhibits large positive activity. All of these results demonstrate the usefulness of BigSTeP in extracting inspiring hypotheses from big databases in a data-driven way.

1. Introduction

Over the past decade, resting-state (or spontaneous) brain activities have attracted great interest from the neuroscience community.

In nonhuman studies, spontaneous brain activities have been reported to include repetitive spatiotemporal patterns (e.g. Ikegaya et al., 2004). Here, spatiotemporal patterns are defined as activities represented by two-dimensional matrices of channel × time (Fig. 1A). Because such patterns resemble the preceding brain activities during tasks, they are assumed to reflect past experiences embedded in neural circuits (Foster and Wilson, 2006; Han et al., 2008; Ji and Wilson, 2007; Wilson and McNaughton, 1994). Furthermore, Dragoi and Tonegawa (2011,

2013) reported that the spatiotemporal patterns are predictive of future brain activities during tasks, suggesting they contribute to encoding future novel experiences. Theoretical studies have implied that encoding information by spatiotemporal patterns offers advantages in terms of the computational efficiency of pattern recognition and memory capacity (Hopfield, 1995; Izhikevich, 2006). All of these studies highlight the significance of examining spatiotemporal patterns in spontaneous brain activities.

In human studies, functional connectivities of resting-state functional MRI (rsfMRI) have been widely examined (Beckmann et al., 2005; Biswal et al., 1995, 2010; Fox et al., 2005; Fox and Raichle, 2007; Raichle et al., 2001; Smith et al., 2009). Functional connectivity is the correlation of

Fig. 1. Assumption of BigSTeP. (**A**): As with STeP (Takeda et al., 2016), resting-state data of a subject is assumed to contain several unknown spatiotemporal patterns at unknown onsets. Spatiotemporal patterns are defined as activities represented by the two-dimensional matrices of channel × time. (**B**): Schematic representation of Eq. (2). Note that $u_{s,k}(t)$ takes a binary (0 or 1) value.

fMRI time series across regions, and it is analyzed using either seed-based correlation (Biswal et al., 2010) or independent component analysis (ICA) (Beckmann et al., 2005). Several sets of correlated brain regions, or resting-state networks (RSNs), have been identified, such as the default mode network (DMN) (Fox et al., 2005; Raichle et al., 2001).

On the other hand, the dynamics of rsfMRIs at a shorter time scale have been examined based on various features, such as dynamic functional connectivity (Allen et al., 2014; Xie et al., 2019) and co-activation pattern (CAP) (Liu et al., 2013, 2018; Liu and Duyn, 2013). Dynamic functional connectivity reveals short-term temporal changes in functional connectivity, and CAPs reveal repetitive spatial patterns representing co-occurring activities. Furthermore, repetitive spatiotemporal patterns have also been estimated from rsfMRIs. By using a template-matching algorithm, Majeed et al. (2011) revealed spatiotemporal patterns involving activation alternating between areas comprising the DMN and the task-positive network. Recently, we developed a method to estimate repetitive spatiotemporal patterns from resting-state brain activity data (SpatioTemporal Pattern estimation, STeP) (Takeda et al., 2016). Without needing the information of onsets, STeP can estimate several spatiotemporal patterns even if they are overlapping. By applying STeP to rsfMRIs, we revealed spatiotemporal patterns that are assumed to represent propagating fMRI activities along the cerebral blood flow.

Nowadays, a growing number of rsfMRIs are publicly available from such databases as the Autism Brain Imaging Data Exchange (ABIDE) (http://fcon_1000.projects.nitrc.org/indi/abide/) and the Human Connectome Project (HCP) (https://www.humanconnectome.org/). ABIDE I provides 1,112 subjects' rsfMRIs, including subjects with autism

spectrum disorder (ASD) and typically developed (TD) individuals, while HCP Young Adult provides over 1,100 subjects' rsfMRIs along with various behavioral data. Such big databases have promoted a better understanding of rsfMRIs. For example, the functional connectivities common across subjects were revealed by using group ICA. In this method, ICA is applied to all sets of rsfMRIs concatenated across all subjects (Calhoun et al., 2001; Smith et al., 2009), providing robust knowledge on functional connectivity. Furthermore, by combining group ICA with dual regression, the individual differences of the functional connectivities were examined (Biswal et al., 2010; Nickerson et al., 2017). In this procedure, IC maps obtained by group ICA are used as templates to identify the corresponding IC maps in each subject. The obtained subject-specific IC maps enable us to examine the relationship between functional connectivity and brain functions.

Likewise, estimating spatiotemporal patterns from such big databases will provide robust knowledge on the spatiotemporal dynamics of rsfMRIs and their functions. However, STeP is not suitable for analyzing many subjects' resting-state data. To estimate the spatiotemporal patterns that are common across subjects, STeP must be applied to very long data concatenated across subjects. This requires a huge amount of memory to store the concatenated data and a long time to search for the onsets of the spatiotemporal patterns.

In this study, we extend STeP so that it can be applied to big databases (BigSTeP). From many subjects' resting-state data, BigSTeP estimates spatiotemporal patterns that are common across subjects (common spatiotemporal patterns) and the corresponding spatiotemporal patterns in each subject (subject-specific spatiotemporal patterns). In BigSTeP, multiple subjects' data are handled separately, so its required memory

can be reduced to that of a single subject. Furthermore, BigSTeP searches for the onsets of the spatiotemporal patterns for each subject, which limits the search space of the onsets and reduces the computation time needed to solve the optimization problem. After verifying the performance of BigSTeP by simulation tests, we applied BigSTeP to over 1,000 subjects' rsfMRIs obtained from ABIDE I. This revealed two common spatiotemporal patterns and the corresponding subject-specific spatiotemporal patterns. We examined the relationships between these patterns and RSNs. Then, we examined the differences in patterns between ASDs and TDs. All of the above analyses demonstrate the usefulness of BigSTeP for extracting inspiring hypotheses from big databases in a data-driven way.

2. BigSTeP

In this section, we propose BigSTeP by extending STeP.

2.1. Assumptions

As with STeP (Takeda et al., 2016), BigSTeP assumes that the resting-state data of a subject contains several unknown spatiotemporal patterns at unknown onsets (Fig. 1A), which is expressed as

$$y_s^{(ch)}(t) = \sum_{k=1}^{K} \sum_{i}^{I_{s,k}} p_{s,k}^{(ch)}(t - \tau_{s,k,i} + 1) + v_s^{(ch)}(t), \tag{1}$$

where $y_s^{(ch)}(t)$ is resting-state data of subject s at channel ch, $p_{s,k}^{(ch)}(t)$ is the k-th spatiotemporal pattern of subject s, called the subject-specific spatiotemporal pattern, K is the number of spatiotemporal patterns, $I_{s,k}$ is the number of onsets for $p_{s,k}^{(ch)}(t)$, $\tau_{s,k,i}$ is the i-th onset of $p_{s,k}^{(ch)}(t)$, and $v_s^{(ch)}(t)$ is noise. $y_s^{(ch)}(t)$ can be various modalities, such as fMRI, magnetoencephalography (MEG), electroencephalography (EEG), and electrocorticography (ECoG). In the case of fMRI, ch represents a voxel or a region of interest (ROI). We assume that the intervals between onsets of different spatiotemporal patterns are variable. Otherwise, for example, if spatiotemporal pattern 1 always appears with a fixed delay after 2, BigSTeP cannot distinguish the two patterns but estimates them as a single spatiotemporal pattern.

By introducing onset time series

$$u_{s,k}(t) = \begin{cases} 1 & t \in \left[\tau_{s,k,1}, \cdots, \tau_{s,k,I_{s,k}} \right] \\ 0 & \text{Otherwise,} \end{cases}$$

Eq. (1) can be rewritten in a convolution form as

$$y_s^{(ch)}(t) = \sum_{k=1}^{K} \sum_{n=1}^{N} p_{s,k}^{(ch)}(n) u_{s,k}(t - n + 1) + v_s^{(ch)}(t), \tag{2}$$

where N is the length of spatiotemporal patterns (Fig. 1B).

Furthermore, BigSTeP assumes that $p_{s,k}^{(ch)}(t)$ contains the pattern that is common across subjects, called the common spatiotemporal pattern, and expresses $p_{s,k}^{(ch)}(n)$ as

$$p_{s,k}^{(ch)}(t) = p_k^{(ch)}(t) + \delta p_{s,k}^{(ch)}(t), \tag{3}$$

where $p_k^{(ch)}(t)$ is the common spatiotemporal pattern and $\delta p_{s,k}^{(ch)}(t)$ is the deviation from it. $\delta p_{s,k}^{(ch)}(t)$ is assumed to be small relative to $p_k^{(ch)}(t)$.

2.2. Purpose

Given the number K and length N of the spatiotemporal patterns,

BigSTeP estimates the common spatiotemporal patterns $\boldsymbol{p}$, the subject-specific spatiotemporal patterns $\boldsymbol{p_s}$, and their onsets $\boldsymbol{u}$ from multi-subject resting-state data $\boldsymbol{y}$, where

$$\boldsymbol{p} = \left\{ p_k^{(ch)}(t) \middle| k = 1 : K, ch = 1 : CH, t = 1 : N \right\},$$
$$\boldsymbol{p_s} = \left\{ p_{s,k}^{(ch)}(t) \middle| s = 1 : S, k = 1 : K, ch = 1 : CH, t = 1 : N \right\},$$
$$\boldsymbol{u} = \left\{ u_{s,k}(t) \middle| s = 1 : S, k = 1 : K, t = 1 : T_s \right\},$$
$$\boldsymbol{y} = \left\{ y_s^{(ch)}(t) \middle| s = 1 : S, ch = 1 : CH, t = 1 : T_s \right\}.$$

Here, $x = 1 : X$ represents $x = 1, \cdots, X$, CH is the number of channels, S is the number of subjects, and T_s is the data length of subject s, which can be different across subjects.

2.3. Objective function

Eq. (2) is rewritten in a matrix form as

$$Y_s = U_s P_s + V_s. \tag{4}$$

Y_s is the $(T_s - N + 1) \times CH$ data matrix expressed as

$$Y_s = \begin{bmatrix} y_s^{(1)}(T_s) & \cdots & y_s^{(CH)}(T_s) \\ y_s^{(1)}(T_s - 1) & \cdots & y_s^{(CH)}(T_s - 1) \\ \vdots & \cdots & \vdots \\ y_s^{(1)}(N) & \cdots & y_s^{(CH)}(N) \end{bmatrix}.$$

U_s is the $(T_s - N + 1) \times (N \times K)$ matrix in which the time-lagged versions of the onset time series are concatenated across k, and it is expressed as

$$U_s = \begin{bmatrix} u_{s,1}(T_s) & \cdots & u_{s,1}(T_s - N + 1) & \cdots & u_{s,K}(T_s) & \cdots & u_{s,K}(T_s - N + 1) \\ u_{s,1}(T_s - 1) & \cdots & u_{s,1}(T_s - N) & \cdots & u_{s,K}(T_s - 1) & \cdots & u_{s,K}(T_s - N) \\ \vdots & \cdots & \vdots & \cdots & \vdots & \cdots & \vdots \\ u_{s,1}(N) & \cdots & u_{s,1}(1) & \cdots & u_{s,K}(N) & \cdots & u_{s,K}(1) \end{bmatrix}.$$

P_s is the $(N \times K) \times CH$ matrix in which the subject-specific spatiotemporal patterns are concatenated across k, and it is expressed as

$$P_s = \begin{bmatrix} p_{s,1}^{(1)}(1) & \cdots & p_{s,1}^{(CH)}(1) \\ \vdots & \cdots & \vdots \\ p_{s,1}^{(1)}(N) & \cdots & p_{s,1}^{(CH)}(N) \\ \vdots & \cdots & \vdots \\ p_{s,K}^{(1)}(1) & \cdots & p_{s,K}^{(CH)}(1) \\ \vdots & \cdots & \vdots \\ p_{s,K}^{(1)}(N) & \cdots & p_{s,K}^{(CH)}(N) \end{bmatrix}.$$

V_s is the $(T_s - N + 1) \times CH$ noise matrix expressed as

$$V_s = \begin{bmatrix} v_s^{(1)}(T_s) & \cdots & v_s^{(CH)}(T_s) \\ v_s^{(1)}(T_s - 1) & \cdots & v_s^{(CH)}(T_s - 1) \\ \vdots & \cdots & \vdots \\ v_s^{(1)}(N) & \cdots & v_s^{(CH)}(N) \end{bmatrix}.$$

Eq. (3) is rewritten in a matrix form as

$$P_s = P + \Delta P_s. \tag{5}$$

P is the $(N \times K) \times CH$ matrix in which the common spatiotemporal patterns are concatenated across k, and it is expressed as
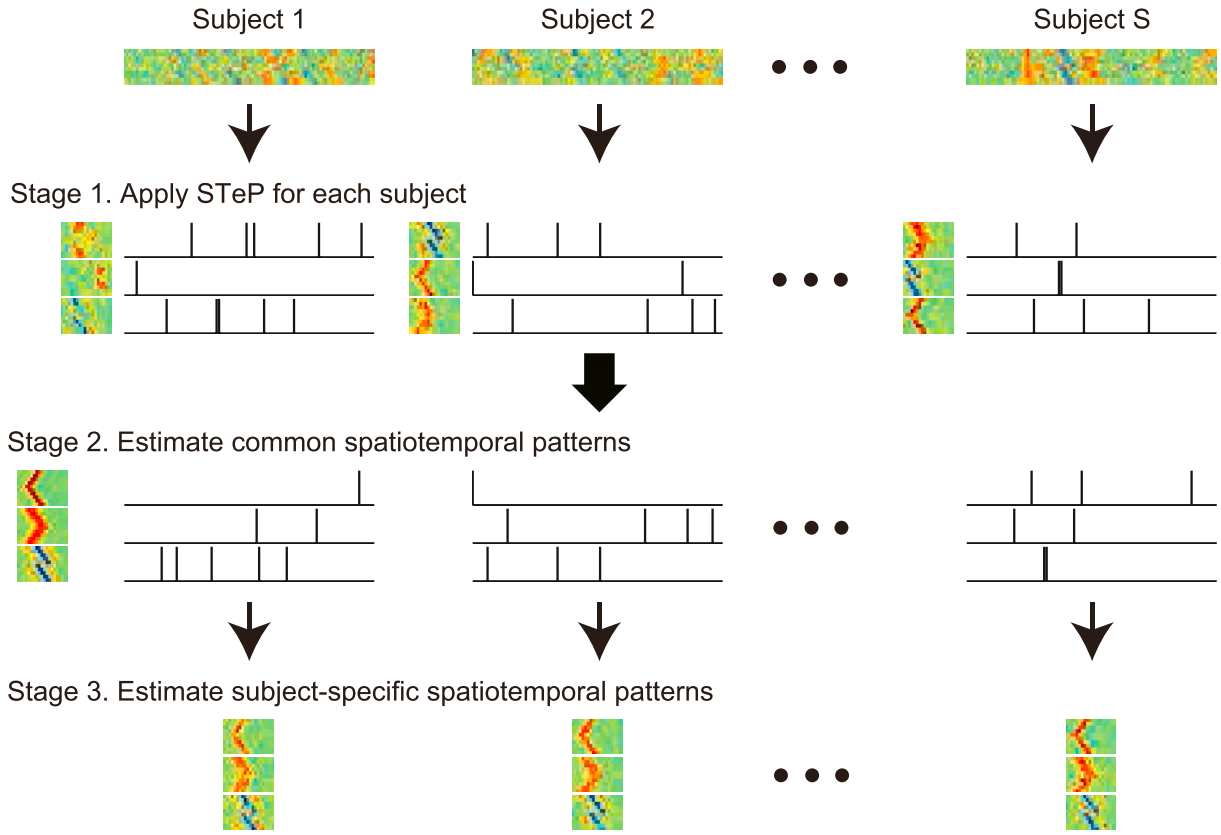
Fig. 2. Procedure of BigSTeP for estimating common and subject-specific spatiotemporal patterns from multi-subject resting-state data. In 1, for each subject, we apply STeP to estimate spatiotemporal patterns and their onsets. In 2, from estimation results of stage 1, we estimate common spatiotemporal patterns and their onsets. In 3, we estimate subject-specific spatiotemporal patterns using onsets estimated in stage 2.

$$P = \begin{bmatrix} p_1^{(1)}(1) & \cdots & p_1^{(CH)}(1) \\ \vdots & \cdots & \vdots \\ p_1^{(1)}(N) & \cdots & p_1^{(CH)}(N) \\ \vdots & \cdots & \vdots \\ p_K^{(1)}(1) & \cdots & p_K^{(CH)}(1) \\ \vdots & \cdots & \vdots \\ p_K^{(1)}(N) & \cdots & p_K^{(CH)}(N) \end{bmatrix}.$$

ΔP_s is the $(N \times K) \times CH$ matrix containing the deviations of the subject-specific spatiotemporal patterns from the common ones, and it is expressed as

$$\Delta P_s = \begin{bmatrix} \delta p_{s,1}^{(1)}(1) & \cdots & \delta p_{s,1}^{(CH)}(1) \\ \vdots & \cdots & \vdots \\ \delta p_{s,1}^{(1)}(N) & \cdots & \delta p_{s,1}^{(CH)}(N) \\ \vdots & \cdots & \vdots \\ \delta p_{s,K}^{(1)}(1) & \cdots & \delta p_{s,K}^{(CH)}(1) \\ \vdots & \cdots & \vdots \\ \delta p_{s,K}^{(1)}(N) & \cdots & \delta p_{s,K}^{(CH)}(N) \end{bmatrix}.$$

By replacing P_s in Eq. (4) with Eq. (5), Eq. (4) can be rewritten as

$$Y_s = U_s P + W_s,$$

where

$$W_s = U_s \Delta P_s + V_s.$$

BigSTeP searches for the common spatiotemporal patterns P and their onsets $U = \{U_s | s = 1 : S\}$ that minimize the sum of all subjects' powers of the residual errors defined as

$$R(P, U) = \sum_{s=1}^{S} \left\| Y_s - U_s P \right\|^2. \tag{6}$$

In this objective function, the power of the residual error is separately calculated for each subject. This removes the need to concatenate data across subjects from the entire procedure of BigSTeP and reduces the necessary memory to that of a single subject.

Furthermore, using the estimated U_s, BigSTeP estimates the subject-specific spatiotemporal patterns P_s that minimize subject s's power of the residual error defined as

$$R_s(P_s) = \| Y_s - U_s P_s \|^2. \tag{7}$$

2.4. Procedure

The procedure of BigSTeP consists of three stages (Fig. 2). In stage 1, for each subject, we apply STeP to estimate spatiotemporal patterns and their onsets. In stage 2, from the estimation results of stage 1, we estimate the common spatiotemporal patterns P and their onsets U. In stage 3, we estimate the subject-specific spatiotemporal patterns P_s using the estimated U_s. These three stages are described below.

Stage 1: For each subject, we apply STeP to estimate spatiotemporal patterns and their onsets. The obtained results are used as the initial values in stage 2.

Stage 2: From the estimation results of stage 1, we estimate P and U by solving the optimization problem of Eq. (6). This procedure is shown in Fig. 3.
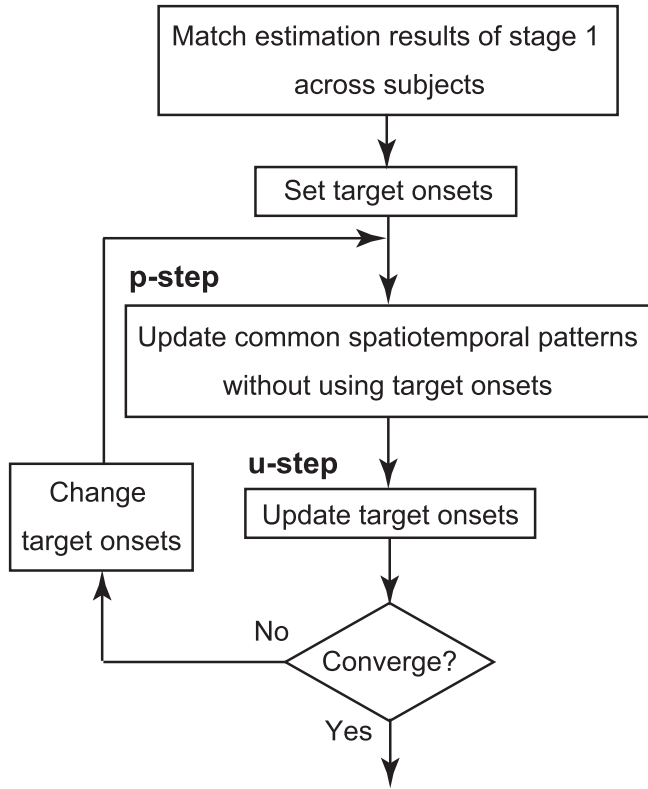
Fig. 3. Flowchart to estimate common spatiotemporal patterns in stage 2. First, the estimation results of stage 1 are matched across subjects so that the order and onsets of spatiotemporal patterns become identical across subjects. Then, the updating of common spatiotemporal patterns and their onsets are alternately iterated until the magnitude of residual error between observed and reconstructed data stops decreasing.

First, we match the estimation results of stage 1 across subjects. In stage 1, the order and the onsets of the spatiotemporal patterns are arbitrarily determined for each subject (Takeda et al., 2016). As a result, a subject's k-th spatiotemporal pattern at time t does not necessarily correspond to that of another subject. Therefore, we reorder the spatiotemporal patterns and adjust their onsets. We regard the spatiotemporal patterns of a subject as references and then change the order and the onsets of the other subjects' spatiotemporal patterns so that the differences between the reference and the other subjects' spatiotemporal patterns are minimized. The matched onsets are used as the initial values in the following procedure.

Then, we search for the optimal P and U that minimize $R(P, U)$ [Eq. (6)]. Once U is obtained, P that minimizes $R(P, U)$ is calculated by

$$\widehat{P} = \left[\sum_{s=1}^{S} U_s^T U_s \right]^{-1} \sum_{s=1}^{S} U_s^T Y_s. \tag{8}$$

On the other hand, once P is obtained, we can search for the onsets that reduce $R(P, U)$. Therefore, we search for the optimal P and U that minimize $R(P, U)$ by alternately iterating the updates of P and U.

We set all subjects' $\tilde{i}$-th onsets of the $\tilde{k}$-th spatiotemporal pattern as the targets to be updated. We iterate

p-step Update P using these onsets except for the target onsets
u-step Update the target onsets so that the residual error becomes smaller
while changing the target onsets in the increasing order of i and k. These two steps are described below.

At p-step, for each subject, an onset time series not containing the target onset $\tau_{s,\tilde{k},\tilde{i}}$ is generated by

$$\tilde{u}_{s,k}(t) = \begin{cases} 0 & t = \tau_{s,\tilde{k},\tilde{i}} \\ u_{s,k}(t) & \text{Otherwise.} \end{cases}$$

Using $\tilde{u} = \{\tilde{u}_{s,k}(t) | s = 1 : S, k = 1 : K, t = 1 : T_s\}$, $\tilde{p} = \{\tilde{p}_k^{(ch)}(t) | k = 1 : K, ch = 1 : CH, t = 1 : N\}$ is calculated by Eq. (8).

At u-step, we update the target onset for each subject. We calculate a residual error of subject s by

$$r_s^{(ch)}(t) = y_s^{(ch)}(t) - \sum_{k=1}^{K} \sum_{n=1}^{N} \tilde{p}_k^{(ch)}(n) \tilde{u}_{s,k}(t - n + 1).$$

Because the onset time series does not assume the target onset $\tau_{s,\tilde{k},\tilde{i}}$, $\tilde{p}_{\tilde{k}}^{(ch)}(t)$ is expected to remain in $r_s^{(ch)}(t)$ around $\tau_{s,\tilde{k},\tilde{i}}$. Therefore, a candidate time point for the target onset is obtained by

$$t_{can} = \underset{t_0 \in t}{\operatorname{argmin}} \sum_{ch=1}^{CH} \sum_{t=1}^{T_s} \left[r_s^{(ch)}(t) - \tilde{p}_{\tilde{k}}^{(ch)}(t - t_0 + 1) \right]^2,$$

where t is the set of time points between the previous and next onsets of the target onset $[\tau_{s,\tilde{k},\tilde{i}-1} + 1 : \tau_{s,\tilde{k},\tilde{i}+1} - 1]$. The target onset is updated to t_{can} only if

$$\sum_{ch=1}^{CH} \sum_{t=1}^{T_s} \left[r_s^{(ch)}(t) - \tilde{p}_{\tilde{k}}^{(ch)}(t - t_{can} + 1) \right]^2 < \sum_{ch=1}^{CH} \sum_{t=1}^{T_s} r_s^{(ch)}(t)^2.$$

Otherwise, the target onset is removed by assuming the onset is not necessary within t.

The decision of convergence is conducted once in updating all onsets of all subjects. We estimate P using all of the subjects' onsets by Eq. (8) and then calculate $R(P, U)$. We exit the loop if $R(P, U)$ is not smaller than that value at the previous decision.

In stages 1 and 2, the onsets are separately estimated for each subject. This drastically reduces the search space of the onsets compared to estimating the onsets from the concatenated data across subjects. This is because estimating the onsets for each subject limits their range within his/her data, while estimating the onsets from the concatenated data expands the range to all of the subjects' data. In this way, BigSTeP reduces the computational cost needed to solve the optimization problem.
Stage 3: Finally, we estimate P_s using the estimated U_s. P_s that minimizes $R_s(P_s)$ [Eq. (7)] is calculated by

$$\widehat{P}_s = \left[U_s^T U_s \right]^{-1} U_s^T Y_s.$$

2.5. Procedure to determine hyperparameters

As with STeP, BigSTeP has two hyperparameters: the number K and length N of the spatiotemporal patterns. In actual application, we need to set them even though they are unknown. Here, we propose a procedure to determine K and N based on the reproducibility of the common spatiotemporal patterns.

First, we randomly divide subjects into two groups. From each group, we estimate the common spatiotemporal patterns and calculate their correlation coefficient between the groups. This is repeated by changing K and N. Finally, we select the best pair of K and N that achieves the highest correlation coefficient.

3. Materials and methods

3.1. Simulation test

We tested the performances of BigSTeP using simulated data.
Following STeP's simulation test (Takeda et al., 2016), we generated five common spatiotemporal patterns using known functions, such as a hemodynamic response function, while setting their length to 20 and the
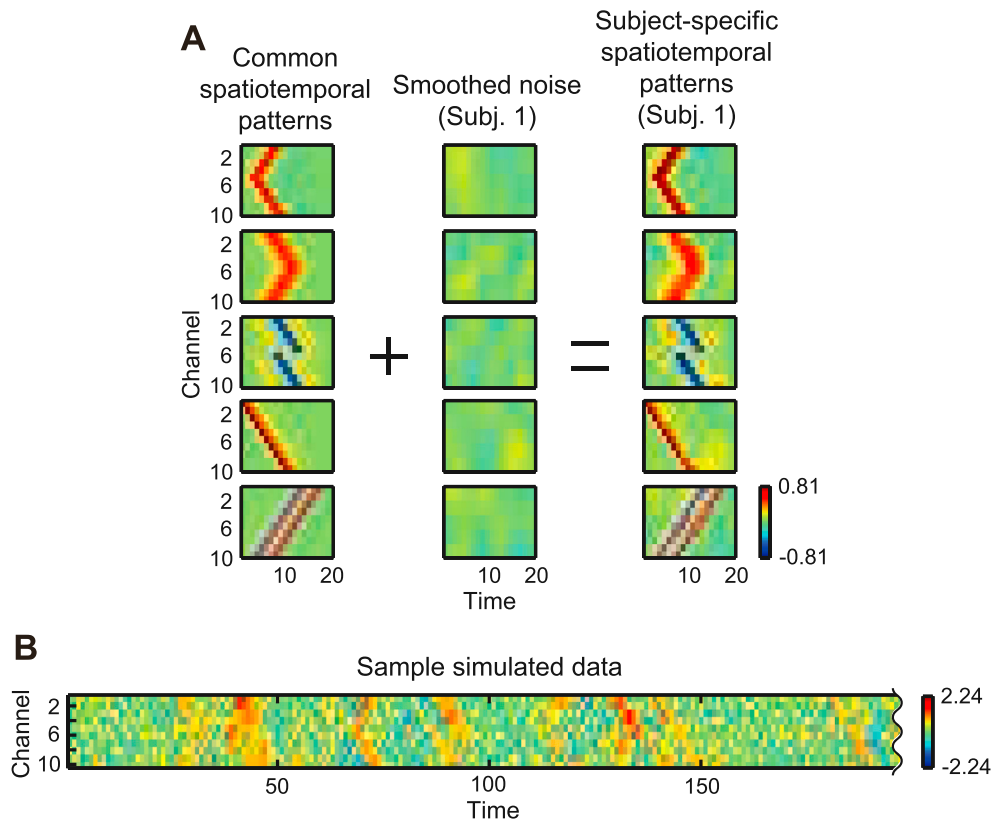
Fig. 4. Simulated data. (**A**): True common and subject-specific spatiotemporal patterns. Subject-specific spatiotemporal patterns were generated by adding smoothed noise to common spatiotemporal patterns. (**B**): Sample simulated data.

number of channels to 10 (Fig. 4A, left). Subject-specific spatiotemporal patterns were generated by adding smoothed Gaussian white noise to the common spatiotemporal patterns (Fig. 4A). The smoothed noise's power was 0.1 times that of the common spatiotemporal patterns. We set the length of simulated data to 1,000 and generated 25 onsets for each pattern using random numbers. From the onsets, the subject-specific spatiotemporal patterns, and Gaussian white noise, we generated simulated data by Eq. (2). The standard deviation (SD) of the noise was 0.40, corresponding to a signal-to-noise ratio (SNR) of −5. The SNR is defined as

$$10\log_{10}\frac{T_s\sum_{ch=1}^{CH}\sum_{t=1}^{N}p_k^{(ch)}(t)^2}{N\sum_{ch=1}^{CH}\sum_{t=1}^{T_s}v_s^{(ch)}(t)^2},$$

where $\sum_{ch=1}^{CH}\sum_{t=1}^{N}p_k^{(ch)}(t)^2$ is the same across k. Fig. 4B shows sample simulated data. In the simulated data, the patterns overlapped each other (Fig. 4B) (Supplementary Material). We generated 10 subjects' simulated data using different onsets and noise. We applied BigSTeP to the 10 subjects' simulated data by setting the number and length of the spatiotemporal patterns to the true values of 5 and 20, respectively. The simulation tests were conducted in 20 runs using different onsets and noise.

Furthermore, we tested the validity of the procedure to determine the two hyperparameters: the number and length of spatiotemporal patterns. We applied BigSTeP to the simulated data by setting the number of spatiotemporal patterns to either 3, 4, 5 (true), 6, or 7 and the length of spatiotemporal patterns to either 10, 20 (true), or 30. For each pair of hyperparameters, we quantified the reproducibility of the estimated common spatiotemporal patterns by comparing them across different runs. We adjusted the order and onsets of the estimated patterns so that the differences in patterns between different runs were minimized, calculated the correlation coefficients of the adjusted patterns, and

averaged the correlation coefficients across the patterns. Finally, the correlation coefficients were averaged across all combinations of the 20 runs.

3.2. Applying BigSTeP to real rsfMRIs

To demonstrate the applicability of BigSTeP to a real dataset, we applied BigSTeP to over 1,000 subjects' rsfMRIs obtained from ABIDE I.

3.2.1. rsfMRIs
We downloaded 1,102 subjects' rsfMRIs that were recorded at 17 international sites and preprocessed with the Data Processing Assistant for Resting-State fMRI (DPARSF) and band-pass filtering (0.01–0.1 Hz). The lengths of the rsfMRIs were 397.65 ± 102.23 s (mean ± SD). The rsfMRIs were normalized to the Montreal Neurological Institute (MNI) template space with a resolution of $3 \times 3 \times 3$ mm^3.

3.2.2. Preprocessing rsfMRIs
We first removed the systemic low-frequency oscillations (sLFOs) (Tong et al., 2012, 2015) from the rsfMRIs using dynamic global signal regression (dGSR) (Erdoğan et al., 2016). We then selected 1,041 subjects (491 ASDs and 550 TDs, 883 males and 158 females, ages 16.62 ± 7.69 years), whose rsfMRIs had non-zero values in all of the gray matter voxels that were defined based on the MNI ICBM 152 template. We extracted the fMRI signals from the gray matter voxels. Although BigSTeP assumes the same sampling rate across subjects, the rsfMRIs were recorded at different sampling rates across the sites (0.33–0.67 Hz). Therefore, we resampled the fMRI time series at 0.5 Hz. Finally, for each voxel we normalized its time series so that it had mean 0 and SD 1.

3.2.3. Applying BigSTeP
To reduce the computation cost, in stages 1 and 2 we reduced the

dimensions of the preprocessed rsfMRIs using singular value decomposition (SVD).

In stage 1, we applied SVD to each subject's rsfMRI, extracted components having the cumulative contribution ratio of 0.99, and multiplied the extracted components by their singular values to keep their amplitude information. This procedure reduced the dimensions from 41,339 to 63.61 ± 17.45. We applied STeP to the dimension-reduced rsfMRIs to estimate the onsets of spatiotemporal patterns.

In stage 2, we applied SVD to all of the subjects' rsfMRIs at once and reduced their dimensions from 41,339 to 9,440 in the same way as described above. SVD was done by performing the eigenvalue decomposition of $\sum_{s=1}^{S} X_s^T X_s$, where X_s is the rsfMRI of subject s. From the dimension-reduced rsfMRIs, we estimated the onsets of common spatiotemporal patterns.

Finally, from the original rsfMRIs we estimated common and subject-specific spatiotemporal patterns using the estimated onsets.

In stage 2, we matched the estimation results of stage 1 across the subjects using the typical spatiotemporal patterns as references. From the 1,041 subjects, we randomly extracted 100 subjects. Among the extracted subjects, we selected the subject whose patterns had minimum distances with those of the other 99 subjects. We regarded the spatiotemporal patterns of the selected subject as references and adjusted the other 1,040 subjects' estimation results to match the references.

3.2.4. Statistical test of common spatiotemporal patterns

After the estimation, we detected significantly large activities in the estimated common spatiotemporal patterns with a statistical test. For each voxel, time, and pattern, we estimated the p-value under the null hypothesis where its absolute value was not larger than zero. We repeated the estimation of the common spatiotemporal patterns by Eq. (8) for 1,000 times while randomly shuffling the inter-onset intervals (IOIs) of the estimated onsets and thus obtained 1,000 null values. The p-value was estimated by

$$p = \frac{\#\{|x0_g| \geq |x|, g = 1 : 1000\}}{1000}, \tag{9}$$

where x and $x0_g$ are the original and g-th null values, respectively.

This is the multiple comparison problem, which we solved by controlling the false discovery rate (FDR). FDR manages the expected proportion of false positive findings among all rejected null hypotheses (Benjamini and Hochberg, 1995). We estimated the q-values by Storey and Tibshirani's method (2003). From the distribution of the p-values,
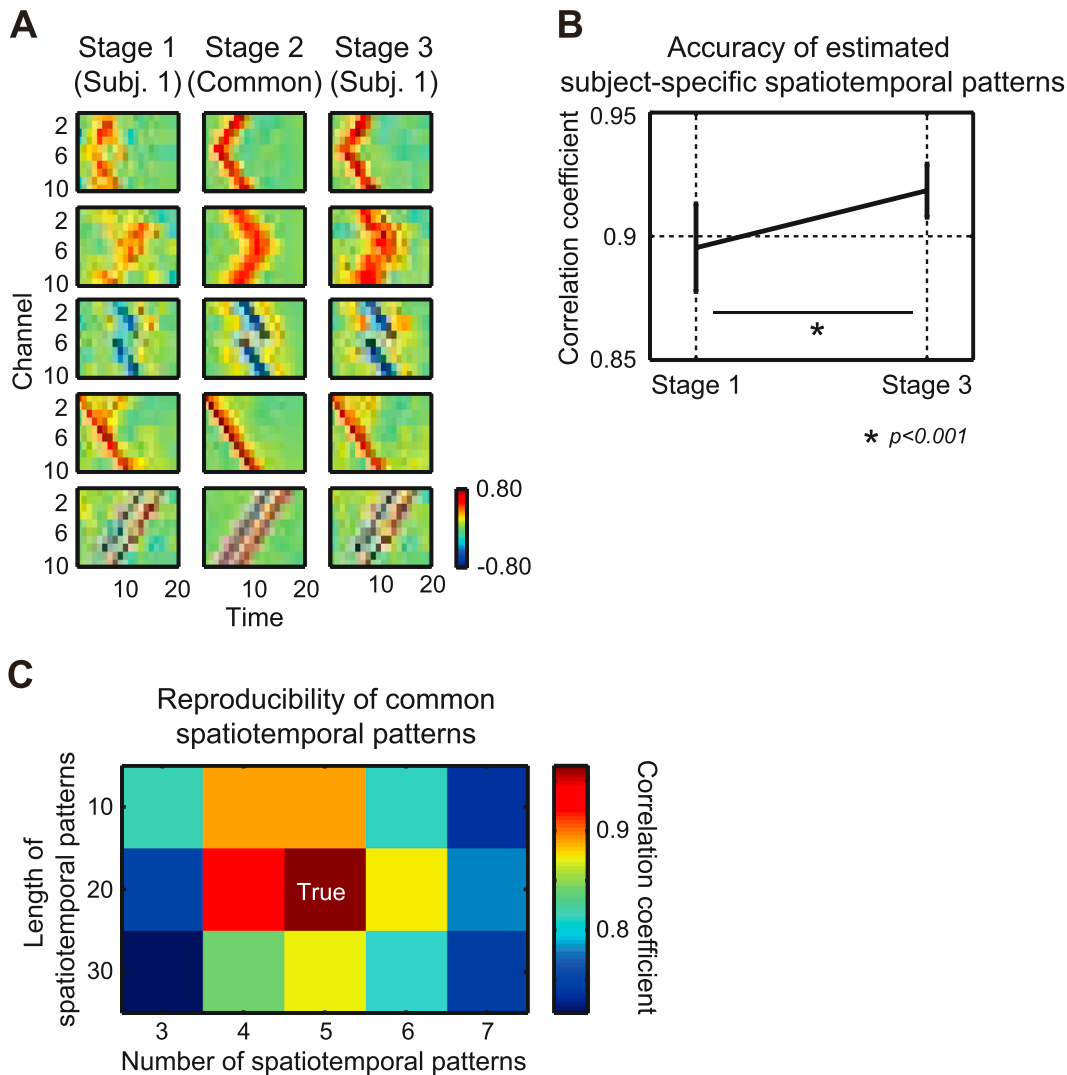
Fig. 5. Results of simulation tests. (**A**): Examples of estimated spatiotemporal patterns at each stage. (**B**): Estimation accuracy of subject-specific spatiotemporal patterns for stages 1 and 3. Correlation coefficients between true and estimated subject-specific spatiotemporal patterns are shown. Error bars represent their SDs across runs. (**C**): Reproducibility of common spatiotemporal patterns for each pair of hyperparameters: number and length of spatiotemporal patterns. Correlation coefficients of estimated common spatiotemporal patterns between different runs are shown.

we first estimated the proportion of the null *p*-values π_0, and based on π_0 we converted the *p*-values to *q*-values. The FDRs were controlled at 0.01.

3.2.5. Examining similarity with resting-state networks

To examine the similarity between the common spatiotemporal patterns and RSNs, we calculated the dot products between them. Ten spatial patterns of RSNs were downloaded from BrainMap ICA (http://brainmap.org/icns/) and normalized to have norm 1. We calculated the dot products between the common spatiotemporal patterns at each time and the spatial patterns of the RSNs.

3.2.6. Examining differences between ASDs and TDs

Using the subject-specific spatiotemporal patterns, we examined the differences between ASDs and TDs by a statistical test. For each time, voxel, and pattern, we compared the values between the groups to produce the *t*-value. Then, we estimated the *p*-value for the *t*-value by a permutation test. We generated 1,000 null *t*-values by shuffling the assignment of the subjects to the groups. From the original and the 1,000 null *t*-values, we estimated the *p*-value by Eq. (9). Lastly, the *p*-values were converted to the *q*-values by Storey and Tibshirani's method (2003). The FDRs were controlled at 0.01.

4. Results

4.1. Simulation test

We tested the performances of BigSTeP using the simulated data (Fig. 4).

Fig. 5A shows examples of the estimated spatiotemporal patterns at each stage. To evaluate the estimation accuracy of the common spatiotemporal patterns, we calculated the correlation coefficients between the true and estimated common spatiotemporal patterns. As a result, we obtained high correlation coefficients (0.98 ± 0.01), indicating that BigSTeP successfully estimated the common spatiotemporal patterns. Furthermore, for stages 1 and 3, we calculated the correlation coefficients between the true and estimated subject-specific spatiotemporal patterns and averaged them across subjects. The correlation coefficients of stage 3 were significantly higher than those of stage 1 ($p < 0.001$, two-tailed Wilcoxon signed-ranks test) (Fig. 5B). This suggests that combining data across subjects by BigSTeP improved the estimation accuracy of the subject-specific spatiotemporal patterns.

We tested the validity of the procedure to determine the two hyperparameters: the number and length of spatiotemporal patterns. Fig. 5C shows the correlation coefficient of the estimated common spatiotemporal patterns across different runs. The correlation coefficient was the highest when we assumed the number and length of the spatiotemporal patterns to be the true values of 5 and 20, respectively. This shows that the most reproducible common spatiotemporal patterns were estimated when we assumed the true values for the hyperparameters. This result suggests the validity of determining the hyperparameters based on the reproducibility of the estimated common spatiotemporal patterns.

In summary, these results demonstrate the validity of BigSTeP.

4.2. Applying BigSTeP to real rsfMRIs

To demonstrate the usefulness of BigSTeP for a real dataset, we applied BigSTeP to the 1,041 subjects' rsfMRIs obtained from ABIDE I.

4.2.1. Determining hyperparameters

To determine the number and length of spatiotemporal patterns, we first examined the reproducibility of the estimated common spatiotemporal patterns. We randomly divided TDs into two groups and estimated the common spatiotemporal patterns separately while setting the number of spatiotemporal patterns to either 1, 2, 3, 4, or 5 and the length of spatiotemporal patterns to either 8, 10, 12, 14, 16, 18, or 20 s. We calculated the correlation coefficients of the estimated common

spatiotemporal patterns between the groups and averaged them across the patterns. This procedure was repeated 10 times, and then we averaged the correlation coefficients.

Fig. 6 shows the resultant correlation coefficients. When the number and length of spatiotemporal patterns were set to 2 and 8 s, respectively, the correlation coefficients exhibited the maximum value of 0.92. Therefore, we set the number and length of spatiotemporal patterns to these values.

4.2.2. Estimated common spatiotemporal patterns

We applied BigSTeP to all of the subjects' rsfMRIs. Fig. 7A shows the estimated common spatiotemporal patterns.

We checked the consistency of the patterns across the subjects. For each subject and pattern, we calculated the correlation coefficient between the common and subject-specific spatiotemporal patterns. The correlation coefficients were sufficiently high (Fig. 7B), indicating that the patterns were consistent across the subjects.

We examined how frequently the patterns appeared in the rsfMRIs. For each subject and pattern, we calculated the number of estimated onsets per minute. As a result, the numbers were about 4 (Fig. 7C), indicating that the patterns appeared about 4 times per minute. Their SDs were sufficiently small (0.80 and 0.82 for patterns 1 and 2, respectively), indicating that the patterns were not concentrated in a small portion of the subjects but ubiquitously appeared in all of the subjects' rsfMRIs.

To examine the similarity between the common spatiotemporal patterns and the RSNs, we calculated the dot products between them. The default mode, sensorimotor, auditory, and visual networks exhibited large values (Fig. 7D), indicating that the patterns contained spatial patterns resembling these networks. These results suggest that the networks are time-locked with each other, consistent with the studies showing that the default mode and task-positive networks are anti-correlated (Fox et al., 2005; Medaglia et al., 2018).

4.2.3. Relationships among common spatiotemporal patterns

In Fig. 7D, the two common spatiotemporal patterns seem to be reversed in time and sign. Pattern 1 exhibits positive activity in the DMN followed by negative activities in the visual networks. In contrast, pattern 2 exhibits positive activities in the visual networks followed by negative activities in the DMN. To confirm this observation, we compared pattern 1 with the minus of time-reversed pattern 2 (Fig. 8), which was generated
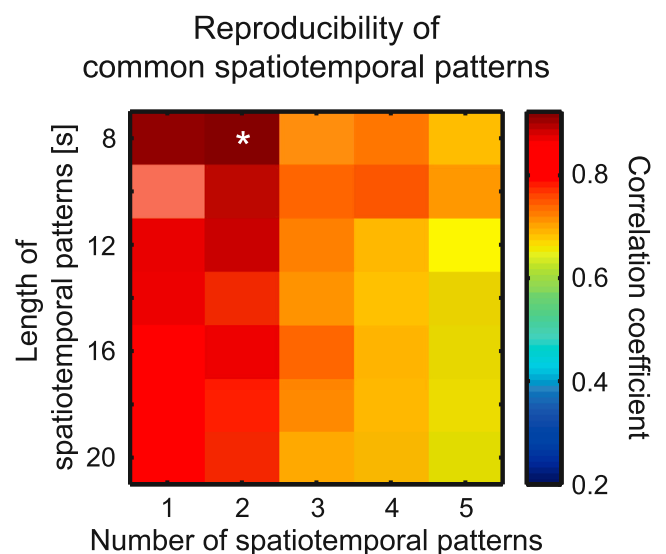
Fig. 6. Reproducibility of common spatiotemporal patterns for each pair of hyperparameters (i.e., number and length of spatiotemporal patterns). Correlation coefficients of estimated common spatiotemporal patterns between two TD groups are shown.
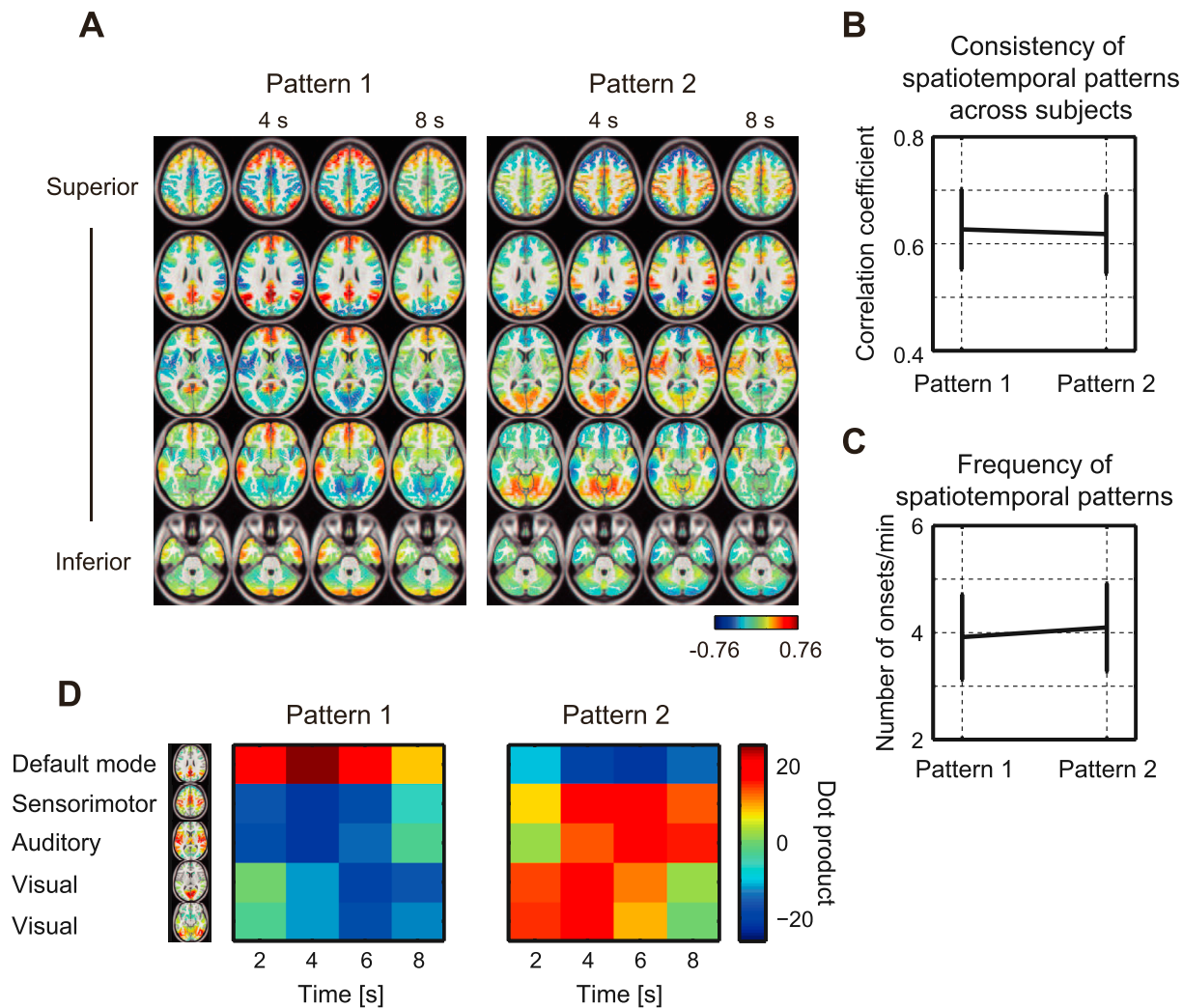
Fig. 7. Spatiotemporal patterns estimated from rsfMRIs of ABIDE I. (**A**): Common spatiotemporal patterns. Significantly large activities are shown ($q < 0.01$). (**B**): Consistency of spatiotemporal patterns across subjects. Correlation coefficients between common and subject-specific spatiotemporal patterns are shown. Error bars represent their SDs across subjects. (**C**): Frequency of spatiotemporal patterns. Numbers of estimated onsets per minute are shown. Error bars represent their SDs across subjects. (**D**): Similarity between estimated common spatiotemporal patterns and RSNs. Dot products between common spatiotemporal patterns at each time and spatial patterns of RSNs are shown. Spatial patterns of RSNs were normalized to have norm 1.

by flipping pattern 2 in the time direction and multiplying it by -1. As a result, pattern 1 more highly resembled the minus of time-reversed pattern 2 (their correlation coefficient was 0.97) than the minus of pattern 2 (correlation coefficient: 0.80). These results suggest that the fMRI activities with opposite signs tend to propagate in the reverse order.

It is possible that the artifacts from BigSTeP or dGSR generated these results. To exclude this possibility, we conducted the same analysis using the averaging procedure and non-GSR rsfMRIs, to which neither GSR nor dGSR was applied. To extract waveforms appearing at the estimated onsets, we averaged the non-GSR rsfMRIs triggering at the onsets. The averaged rsfMRIs triggering at pattern 1 and 2's onsets are respectively called averages 1 and 2. Average 1 more highly resembled the minus of time-reversed average 2 (correlation coefficient: 0.96) than the minus of average 2 (correlation coefficient: 0.81). These results also support the suggestion that the fMRI activities with opposite signs tend to propagate in the reverse order.

4.2.4. Estimated onsets of spatiotemporal patterns

To examine the regularity in the onset timing of the patterns, we calculated the auto- and cross-correlograms of the estimated onsets. From the two patterns, we first defined target and trigger patterns. Then, from the onset time series of the target pattern, we extracted 16-sec segments

after the onsets of the trigger pattern and averaged the segments to produce a correlogram. Finally, the correlograms were averaged across the subjects. The resultant correlograms represent the probabilities of the target pattern appearing after the onsets of the trigger pattern with each delay.

Fig. 9 shows the auto- (A and D) and cross-correlograms (B and C), and red lines represents the 100 surrogate correlograms obtained using IOI-shuffled onsets. The auto-correlograms exhibited the lowest peaks at 8 s (Fig. 9A and D), indicating that the same patterns tended to be suppressed at 8 s after their onsets. The cross-correlograms exhibited the highest peaks at 10 s, although the values themselves were low (Fig. 9B and C). This indicates that pattern 1 had a weak but significant tendency to appear after pattern 2, and vice versa.

4.2.5. Differences between ASDs and TDs

We examined the differences in the spatiotemporal patterns between ASDs and TDs.

The artifacts from the subjects' head motions may generate the differences between the groups. To check this possibility, we first compared the magnitudes of the head motions between ASDs and TDs based on the mean framewise displacement "func_mean_fd" in the phenotypic file of ABIDE I. As a result, ASDs exhibited larger head motions than TDs (0.15
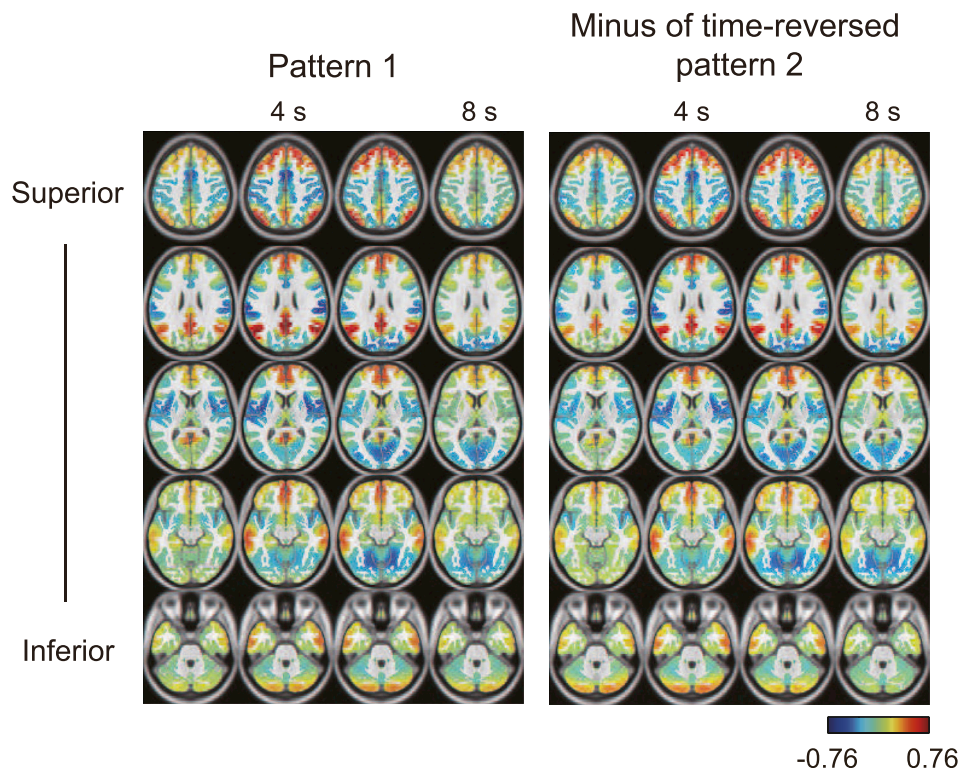
Fig. 8. Relationship between estimated common spatiotemporal patterns. Common spatiotemporal pattern 1 and minus of time-reversed common spatiotemporal pattern 2 are shown.

± 0.19 mm for ASDs and 0.10 ± 0.10 mm for TDs) ($p < 0.001$, two-tailed *t*-test). Power et al. (2012) showed that head motions increase fMRI amplitudes, resulting in spurious functional connectivities. Therefore, it is assumed that the larger head motions in ASDs induced the larger amplitudes in their patterns.

We estimated the common spatiotemporal patterns for ASDs and TDs using their fMRIs and onsets, and then we calculated the differences in their amplitudes (|ASD| − |TD|). Fig. 10A shows the amplitude differences at the significant voxels ($q < 0.01$), and the clusters larger than 200 voxels are enlarged below. The statistical test was conducted by comparing the subject-specific spatiotemporal patterns between ASDs and TDs. Pattern 1 showed smaller amplitudes in ASDs than in TDs at the right prefrontal cortex, the thalamus, and the posterior cingulate cortex (PCC). The smaller amplitudes in ASDs are inconsistent with the expectation from the larger head motions in ASDs, indicating that this result was not generated by the artifacts from the head motions. The right prefrontal cortex, the thalamus, and the PCC agree with the studies that examined the differences in rsfMRIs between ASDs and TDs (Anderson et al., 2011; Di Martino et al., 2014; Itahashi et al., 2015; Lau et al., 2019; Nair et al., 2013; Wang et al., 2018; Yahata et al., 2016).

Information on the significant differences is summarized in Table 1. These differences seem to be concentrated at 4 s in pattern 1. To confirm this observation, for each time and pattern we counted the significant voxels. Fig. 10B shows the number of significant voxels. The largest number of significant voxels was observed at 4 s in pattern 1, when the DMN exhibited large positive activity (Fig. 7D). These results suggest that the differences are context-dependent, that is, the differences in fMRI activities between ASDs and TDs tend to occur when the DMN exhibits large positive activity.

It has been reported that ASDs exhibit under-connectivity within the DMN (Hull et al., 2017; Uddin et al., 2013). Here, we examined whether the differences in the patterns between ASDs and TDs were associated with the under-connectivity. For this purpose, we first reconstructed the fMRIs using the subject-specific spatiotemporal patterns and their onsets by Eq. (2). Using the reconstructed fMRIs, we then calculated the

pairwise correlation coefficients and averaged them within the DMN. The DMN region was defined based on the IC map obtained from BrainMap ICA. Fig. 10C shows the correlation coefficients. The correlation coefficients of ASDs were significantly lower than those of TDs ($p < 0.001$, two-tailed *t*-test) (Fig. 10C, blue line), indicating that the reconstructed fMRIs reproduced the ASD's under-connectivity within the DMN. In contrast, when we reconstructed the fMRIs using the patterns shuffled across the subjects, no under-connectivity of ASDs was observed ($p = 0.36$, two-tailed *t*-test) (Fig. 10C, red line). These results suggest that the differences in the patterns between ASDs and TDs are associated with the ASDs' under-connectivity within the DMN.

5. Discussion

In this study, we extended STeP (Takeda et al., 2016) to BigSTeP so that it could be applied to big databases. From many subjects' resting-state data, BigSTeP estimates common and subject-specific spatiotemporal patterns. The simulation tests show the efficacy of combining multiple subjects' data by BigSTeP. We applied BigSTeP to over 1,000 subjects' rsfMRIs obtained from ABIDE I. This revealed interesting spatiotemporal patterns (Figs. 7–10), suggesting the usefulness of BigSTeP for big databases.

5.1. Methodological considerations

We proposed BigSTeP by extending STeP. The main advantage of BigSTeP over STeP is its ability to handle multiple resting-state data separately. In the case of STeP, we need to concatenate data across subjects to estimate spatiotemporal patterns that are common across subjects. This requires huge memory to store the big matrix (concatenated data) and a long time to search for the onsets of the spatiotemporal patterns. In the case of using BigSTeP, in contrast, we do not need to concatenate data across subjects. This removes the necessity of storing the entire big matrix at a single time and enables us to analyze datasets of any size. Furthermore, because each subject's onsets are searched for

Target pattern
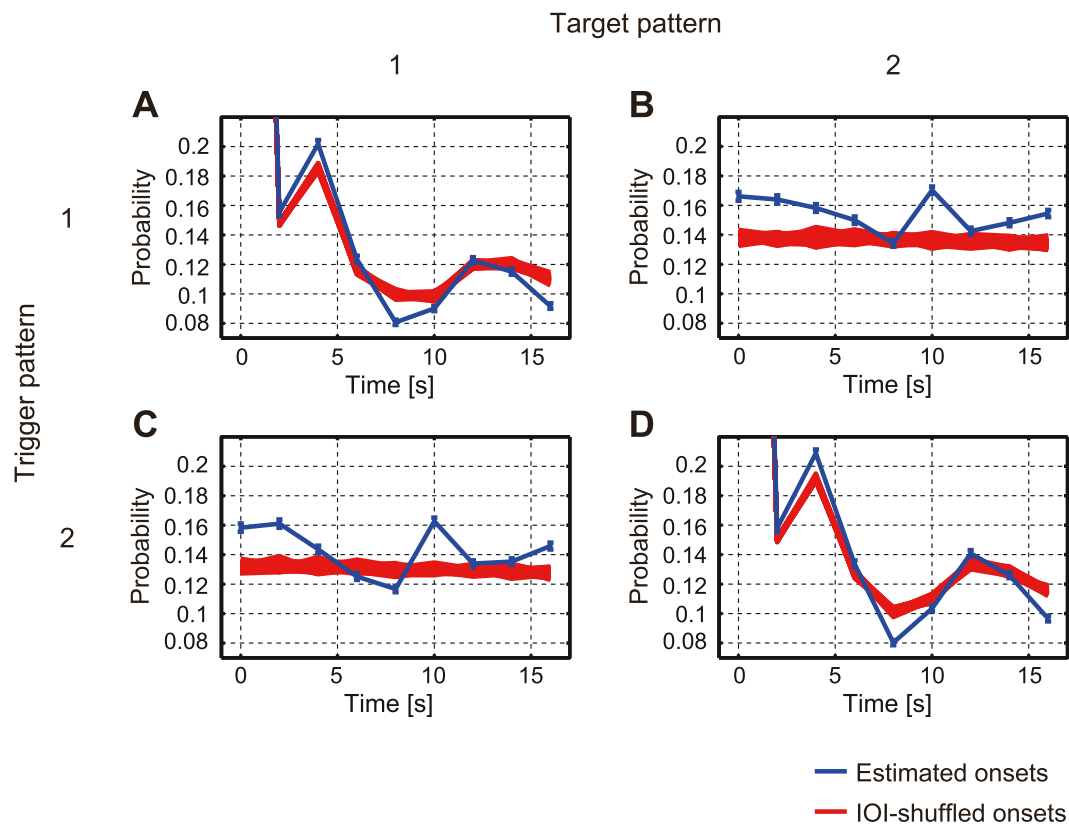
Fig. 9. Auto- and cross-correlograms of estimated onsets. Error bars represent their standard errors across subjects. Blue and red lines, respectively, represent original and 100 surrogate correlograms obtained using IOI-shuffled onsets. (**A**): Auto-correlogram of pattern 1 obtained by averaging onset time series of pattern 1 triggering at onsets of pattern 1. (**B**): Cross-correlogram obtained by averaging onset time series of pattern 2 triggering at onsets of pattern 1. (**C**): Cross-correlogram obtained by averaging onset time series of pattern 1 triggering at onsets of pattern 2. (**D**): Auto-correlogram of pattern 2 obtained by averaging onset time series of pattern 2 triggering at onsets of pattern 2.

separately, the search range of the onsets is narrowed down, reducing the computation time needed for solving the optimization problem.

BigSTeP assumes that all of the spatiotemporal patterns contain common patterns across subjects [Eq. (3)]. However, this assumption is not necessarily true in a real situation. It is possible that some of the patterns are completely different across subjects. In that case, BigSTeP cannot estimate such patterns (Supplementary Material). To check the validity of the assumption, as shown in Fig. 7B, it is preferable to confirm the consistency of the estimated patterns across subjects by calculating the correlation coefficients between common and subject-specific spatiotemporal patterns.

In BigSTeP, we set the same value N for the lengths of all of the spatiotemporal patterns. However, it is not necessary for the actual lengths of all spatiotemporal patterns to be exactly N, and thus they can be variable below N (Supplementary Material). Indeed, the spatiotemporal patterns used in the simulation test had variable lengths below N (Fig. 4A, left).

5.2. Spatiotemporal patterns estimated from ABIDE I

Using BigSTeP, we estimated the spatiotemporal patterns from the rsfMRIs obtained from ABIDE I. The estimated spatiotemporal patterns represent the fMRI activities consecutively changed with time, such as propagating waves (Fig. 7A). Because the subjects include 491 ASDs and 550 TDs with ages of 16.62 ± 7.69 years, the patterns reflect the fMRI activities of these groups mainly in adolescence.

The common spatiotemporal patterns include the spatial patterns resembling those of the default mode, sensorimotor, auditory, and visual

networks (Fig. 7D). This suggests that these networks are time-locked with each other, consistent with the previous studies showing that the default mode and task-positive networks are anticorrelated (Fox et al., 2005; Medaglia et al., 2018).

Using a template-matching algorithm, Majeed et al. (2011) revealed a template of about 16 s, which displays switching between the task-positive and the default mode networks (Fig. 7 in Majeed et al., 2011). Because the two common spatiotemporal patterns also included these networks (Fig. 7A and D), it is assumed that BigSTeP decomposed the 16-sec template into two 8-sec patterns as the common spatiotemporal patterns. Indeed, the cross-correlograms of the estimated onsets indicate that the two patterns were slightly time-locked with each other (Fig. 9B and C).

Common spatiotemporal pattern 1 highly resembled the minus variant of time-reversed common spatiotemporal pattern 2 (Fig. 8), suggesting that fMRI activities with opposite signs propagate in the reverse order. This might be related to a physical phenomenon, that is, the reflection of a pulse at a fixed end. For example, a pulse moving through a string with an upward displacement reached a fixed end and returned with a downward displacement. Indeed, pattern 2 tended to appear after pattern 1, and vice versa (Fig. 9B and C). However, the detailed mechanism underlying this result remains to be elucidated.

By comparing the spatiotemporal patterns between ASDs and TDs, we examined the observed differences between the groups (Fig. 10). The rsfMRIs were recorded at different sites (17 sites), and different sites were reported to have different measurement biases (Yamashita et al., 2019). Therefore, it is possible that the measurement biases generated the differences in patterns between ASDs and TDs if the groups were
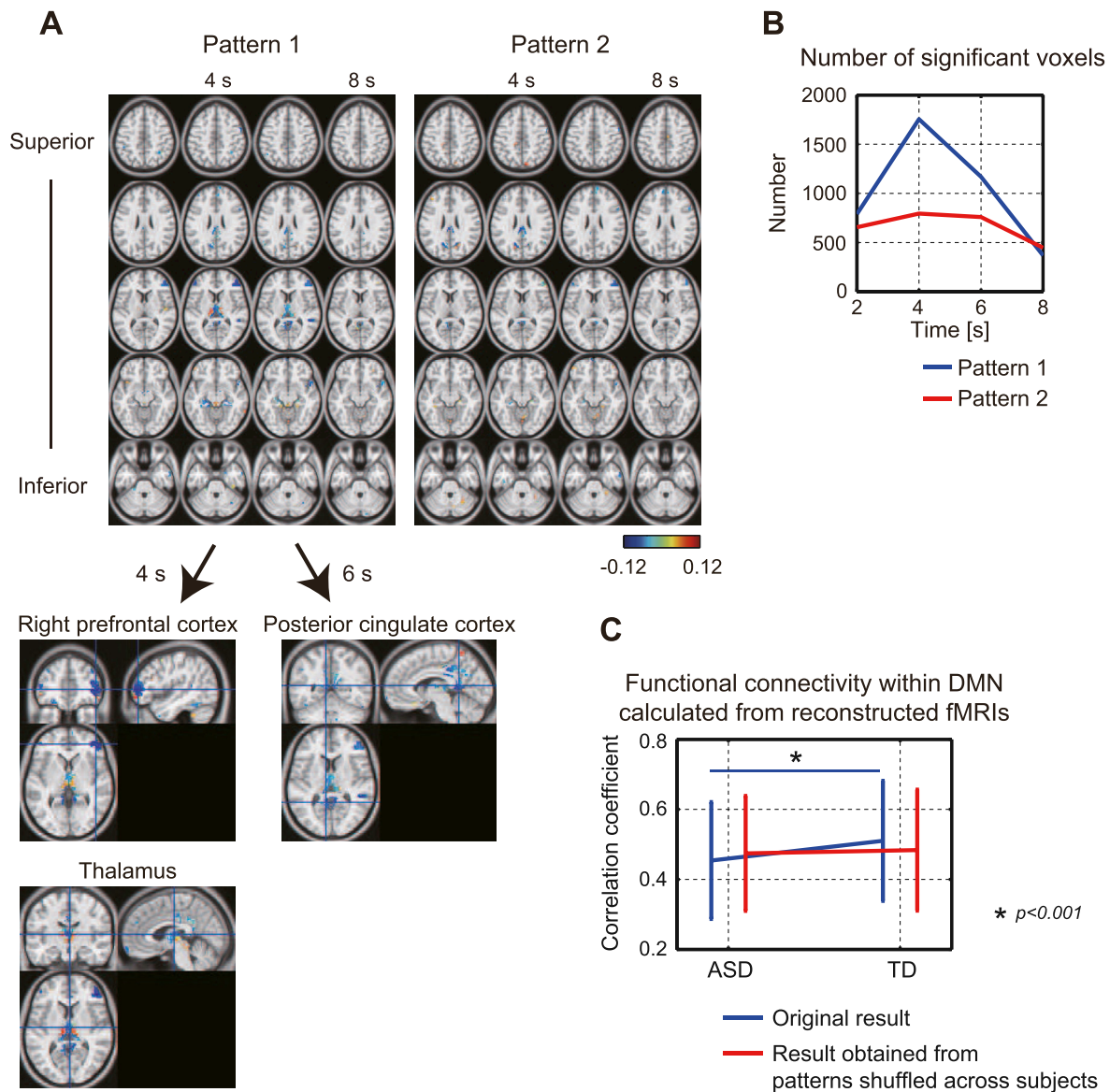
Fig. 10. Differences in spatiotemporal patterns between ASDs and TDs. (**A**): Amplitude differences among common spatiotemporal patterns (|ASD| − |TD|) at significant voxels ($q < 0.01$). Negative values indicate that amplitudes of ASDs are smaller than those of TDs. Clusters larger than 200 voxels are enlarged below. (**B**): Number of significant voxels ($q < 0.01$). (**C**): Functional connectivity within DMN calculated from reconstructed fMRIs using subject-specific spatiotemporal patterns and their onsets. Pairwise correlation coefficients averaged within DMN are shown. Error bars represent their SDs across subjects.

biased across the sites. However, this is not the case with ABIDE I because the numbers of ASDs and TDs were balanced at each site (Di Martino et al., 2014).

At the right prefrontal cortex, the thalamus, and the PCC in pattern 1, ASDs exhibited smaller amplitudes than did TDs (Fig. 10A). The smaller amplitudes in ASDs are inconsistent with the expectation from the larger head motions in ASDs (Power et al., 2012), indicating that this result was not generated by the artifacts from the head motions. Results for the right prefrontal cortex, the thalamus, and the PCC agree with those in the studies that examined the differences in rsfMRIs between ASDs and TDs (Anderson et al., 2011; Di Martino et al., 2014; Itahashi et al., 2015; Lau et al., 2019; Nair et al., 2013; Wang et al., 2018; Yahata et al., 2016). Previously, it has been reported that adolescent and adult ASDs exhibit under-connectivity within the DMN (Hull et al., 2017; Itahashi et al., 2015; Lau et al., 2019; Uddin et al., 2013). Because the fMRIs reconstructed from the patterns reproduced the under-connectivity (Fig. 10C), the smaller amplitudes at the PCC in ASDs (Fig. 10A) are assumed to be

associated with the ASD's under-connectivity within the DMN. The prefrontal cortex and the DMN have been reported to be involved in social cognition (Li et al., 2014; Patriquin et al., 2016), such as the theory of mind (Baron-Cohen, 1988), and ASDs have deficits in social cognition (Hull et al., 2017). Taking these reports into account, the smaller amplitudes at these regions in ASDs (Fig. 10A) are assumed to be associated with their deficits in social cognition.

The differences tended to occur at 4 s in pattern 1 (Fig. 10B), when the DMN exhibited large positive activity (Fig. 7D). This result suggests context-dependent differences: The differences in fMRI activities between ASDs and TDs do not always occur during resting state but tend to occur when the DMN exhibits large positive activity. Positive/negative fMRI activities have been reported to reflect the increase/decrease in neuronal activities (Logothetis et al., 2001; Shmuel et al., 2006). Taking these reports into account, the effect of context-dependent differences is considered reasonable.

In summary, BigSTeP provided inspiring suggestions and hypotheses

Table 1
Differences in spatiotemporal patterns between ASDs and TDs. Peak differences in clusters larger than 100 voxels are shown. Listed here are time [s] in each pattern, region names defined by anatomical automatic labeling (AAL) except for Midbrain L, absolute values of peak *t*-values, MNI coordinates [mm], and signs of amplitude differences (|ASD| − |TD|), where minus indicates a smaller amplitude in ASDs than TDs.

Time [s]	Region	*T*-value	x, y, z	|ASD| − |TD|
Pattern 1				
2	Frontal Inf Tri R	5.55	48, 39, 6	−
2	Frontal Mid Orb R	5.33	42, 45, −6	−
4	Lingual L	6.35	−9, −42, 0	−
4	Frontal Inf Tri R	6.28	48, 39, 3	−
4	ParaHippocampal L	6.26	−18, −36, −12	−
4	Thalamus L	5.78	−3, −24, 3	−
4	Midbrain L	5.25	−3, −24, −15	+
4	Thalamus R	5.16	6, −9, −3	−
4	Cingulum Mid L	4.92	−3, −18, 33	−
4	Cingulum Post L	4.76	−9, −36, 33	−
4	Cingulum Post L	4.38	−6, −45, 18	−
4	Cingulum Mid R	4.25	12, −21, 39	+
6	Cingulum Post R	5.45	6, −45, 9	−
6	Cingulum Post L	5.29	−6, −45, 9	−
6	Frontal Inf Tri R	5.27	45, 39, 6	−
6	Cingulum Mid L	4.86	−9, −27, 39	+
6	Thalamus L	4.57	−6, −6, 9	−
6	Thalamus L	4.25	−3, −24, 6	−
6	Thalamus L	4.19	−12, −30, 9	−
Pattern 2				
Time [s]	Region	*T*-value	x, y, z	|ASD| − |TD|
6	Frontal Inf Orb R	5.95	45, 48, −3	−
8	Frontal Inf Tri R	5.44	45, 42, 0	−

regarding rsfMRIs, implying the usefulness of BigSTeP in data-driven and hypothesis-generating research.

5.3. Applicability

In this paper, we have concentrated on applying BigSTeP to rsfMRIs. It should be mentioned that, as with STeP, BigSTeP can also be applied to resting-state MEG, EEG, and ECoG.

Furthermore, BigSTeP can be applied to very long data, such as sleep EEG. In this case, the long data is divided into short segments, which are regarded as subjects in the BigSTeP framework. From the segmented data, BigSTeP estimates spatiotemporal patterns that are common across the segments as well as the segment-specific spatiotemporal patterns.

A MATLAB implementation of BigSTeP is available at https://bicr.atr.jp//~takeda/BigSTeP.html.

6. Data and code availability statement

Data analyzed in this study are available from Autism Brain Imaging Data Exchange I (ABIDE I) (http://fcon_1000.projects.nitrc.org/indi/abide/abide_I.html). A MATLAB implementation of our method (BigSTeP) is available at https://bicr.atr.jp//~takeda/BigSTeP.html.

Acknowledgments

Appendix A. Supplementary data

Supplementary data to this article can be found online at https://doi.org/10.1016/j.neuroimage.2019.116182.

References

Allen, E.A., Damaraju, E., Plis, S.M., Erhardt, E.B., Eichele, T., Calhoun, V.D., 2014. Tracking whole-brain connectivity dynamics in the resting state. Cerebr. Cortex 24, 663–676. https://doi.org/10.1093/cercor/bhs352.

Anderson, J.S., Nielsen, J.A., Froehlich, A.L., DuBray, M.B., Druzgal, T.J., Cariello, A.N., Cooperrider, J.R., Zielinski, B.A., Ravichandran, C., Fletcher, P.T., Alexander, A.L., Bigler, E.D., Lange, N., Lainhart, J.E., 2011. Functional connectivity magnetic resonance imaging classification of autism. Brain 134, 3742–3754. https://doi.org/10.1093/brain/awr263.

Baron-Cohen, S., 1988. Without a theory of mind one cannot participate in a conversation. Cognition 29, 83–84. https://doi.org/10.1016/0010-0277(88)90011-X.

Beckmann, C.F., DeLuca, M., Devlin, J.T., Smith, S.M., 2005. Investigations into resting-state connectivity using independent component analysis. Philos. Trans. R. Soc. Lond. B Biol. Sci. 360, 1001–1013. https://doi.org/10.1098/rstb.2005.1634.

Benjamini, Y., Hochberg, Y., 1995. Controlling the false discovery rate: a practical and powerful approach to multiple testing. J. R. Stat. Ser. Soc. B Stat. Methodol. 57, 289–300.

Biswal, B.B., Mennes, M., Zuo, X.N., Gohel, S., Kelly, C., Smith, S.M., Beckmann, C.F., Adelstein, J.S., Buckner, R.L., Colcombe, S., Dogonowski, A.M., Ernst, M., Fair, D., Hampson, M., Hoptman, M.J., Hyde, J.S., Kiviniemi, V.J., Kötter, R., Li, S.J., Lin, C.P., Lowe, M.J., Mackay, C., Madden, D.J., Madsen, K.H., Margulies, D.S., Mayberg, H.S., McMahon, K., Monk, C.S., Mostofsky, S.H., Nagel, B.J., Pekar, J.J., Peltier, S.J., Petersen, S.E., Riedl, V., Rombouts, S.A., Rypma, B., Schlaggar, B.L., Schmidt, S., Seidler, R.D., Siegle, G.J., Sorg, C., Teng, G.J., Veijola, J., Villringer, A., Walter, M., Wang, L., Weng, X.C., Whitfield-Gabrieli, S., Williamson, P., Windischberger, C., Zang, Y.F., Zhang, H.Y., Castellanos, F.X., Milham, M.P., 2010. Toward discovery science of human brain function. Proc. Natl. Acad. Sci. U.S.A. 107, 4734–4739. https://doi.org/10.1073/pnas.0911855107.

Biswal, B.B., Yetkin, F.Z., Haughton, V.M., Hyde, J.S., 1995. Functional connectivity in the motor cortex of resting human brain using echo-planar MRI. Magn. Reson. Med. 34, 537–541.

Calhoun, V.D., Adali, T., Pearlson, G.D., Pekar, J.J., 2001. A method for making group inferences from functional MRI data using independent component analysis. Hum. Brain Mapp. 14, 140–151.

Di Martino, A., Yan, C.G., Li, Q., Denio, E., Castellanos, F.X., Alaerts, K., Anderson, J.S., Assaf, M., Bookheimer, S.Y., Dapretto, M., Deen, B., Delmonte, S., Dinstein, I., Ertl-Wagner, B., Fair, D.A., Gallagher, L., Kennedy, D.P., Keown, C.L., Keysers, C., Lainhart, J.E., Lord, C., Luna, B., Menon, V., Minshew, N.J., Monk, C.S., Mueller, S., Müller, R.A., Nebel, M.B., Nigg, J.T., O'Hearn, K., Pelphrey, K.A., Peltier, S.J., Rudie, J.D., Sunaert, S., Thioux, M., Tyszka, J.M., Uddin, L.Q., Verhoeven, J.S., Wenderoth, N., Wiggins, J.L., Mostofsky, S.H., Milham, M.P., 2014. The autism brain imaging data exchange: towards a large-scale evaluation of the intrinsic brain architecture in autism. Mol. Psychiatry 19, 659–667. https://doi.org/10.1038/mp.2013.78.

Dragoi, G., Tonegawa, S., 2011. Preplay of future place cell sequences by hippocampal cellular assemblies. Nature 469, 397–401. https://doi.org/10.1038/nature09633.

Dragoi, G., Tonegawa, S., 2013. Distinct preplay of multiple novel spatial experiences in the rat. Proc. Natl. Acad. Sci. U.S.A. 110, 9100–9105. https://doi.org/10.1073/pnas.1306031110.

Erdoğan, S.B., Tong, Y., Hocke, L.M., Lindsey, K.P., deB Frederick, B., 2016. Correcting for blood arrival time in global mean regression enhances functional connectivity analysis of resting state fMRI-BOLD signals. Front. Hum. Neurosci. 10, 311. https://doi.org/10.3389/fnhum.2016.00311.

Foster, D.J., Wilson, M.A., 2006. Reverse replay of behavioural sequences in hippocampal place cells during the awake state. Nature 440, 680–683. https://doi.org/10.1038/nature04587.

Fox, M.D., Raichle, M.E., 2007. Spontaneous fluctuations in brain activity observed with functional magnetic resonance imaging. Nat. Rev. Neurosci. 8, 700–711. https://doi.org/10.1038/nrn2201.

Fox, M.D., Snyder, A.Z., Vincent, J.L., Corbetta, M., Van Essen, D.C., Raichle, M.E., 2005. The human brain is intrinsically organized into dynamic, anticorrelated functional networks. Proc. Natl. Acad. Sci. U.S.A. 102, 9673–9678. https://doi.org/10.1073/pnas.0504136102.

Han, F., Caporale, N., Dan, Y., 2008. Reverberation of recent visual experience in spontaneous cortical waves. Neuron 60, 321–327. https://doi.org/10.1016/j.neuron.2008.08.026.

Hopfield, J.J., 1995. Pattern recognition computation using action potential timing for stimulus representation. Nature 376, 33–36. https://doi.org/10.1038/376033a0.

Hull, J.V., Dokovna, L.B., Jacokes, Z.J., Torgerson, C.M., Irimia, A., Van Horn, J.D., 2017. Resting-state functional connectivity in autism spectrum disorders: a review. Front. Psychiatry 7, 205. https://doi.org/10.3389/fpsyt.2016.00205.

Ikegaya, Y., Aaron, G., Cossart, R., Aronov, D., Lampl, I., Ferster, D., Yuste, R., 2004. Synfire chains and cortical songs: temporal modules of cortical activity. Science 304, 559–564. https://doi.org/10.1126/science.1093173.

Itahashi, T., Yamada, T., Watanabe, H., Nakamura, M., Ohta, H., Kanai, C., Iwanami, A., Kato, N., Hashimoto, R., 2015. Alterations of local spontaneous brain activity and

connectivity in adults with high-functioning autism spectrum disorder. Mol. Autism. 6, 30. https://doi.org/10.1186/s13229-015-0026-z.

Izhikevich, E.M., 2006. Polychronization: computation with spikes. Neural Comput. 18, 245–282. https://doi.org/10.1162/089976606775093882.

Ji, D., Wilson, M.A., 2007. Coordinated memory replay in the visual cortex and hippocampus during sleep. Nat. Neurosci. 10, 100–107. https://doi.org/10.1038/nn1825.

Lau, W.K.W., Leung, M.K., Lau, B.W.M., 2019. Resting-state abnormalities in autism spectrum disorders: a meta-analysis. Sci. Rep. 9, 3892. https://doi.org/10.1038/s41598-019-40427-7.

Li, W., Mai, X., Liu, C., 2014. The default mode network and social understanding of others: what do brain connectivity studies tell us. Front. Hum. Neurosci. 8, 74. https://doi.org/10.3389/fnhum.2014.00074.

Liu, X., Chang, C., Duyn, J.H., 2013. Decomposition of spontaneous brain activity into distinct fMRI co-activation patterns. Front. Syst. Neurosci. 7, 101. https://doi.org/10.3389/fnsys.2013.00101.

Liu, X., Duyn, J.H., 2013. Time-varying functional network information extracted from brief instances of spontaneous brain activity. Proc. Natl. Acad. Sci. U.S.A. 110, 4392–4397. https://doi.org/10.1073/pnas.1216856110.

Liu, X., Zhang, N., Chang, C., Duyn, J.,H., 2018. Co-activation patterns in resting-state fMRI signals. Neuroimage 180, 485–494. https://doi.org/10.1016/j.neuroimage.2018.01.041.

Logothetis, N.K., Pauls, J., Augath, M., Trinath, T., Oeltermann, A., 2001. Neurophysiological investigation of the basis of the fMRI signal. Nature 412, 150–157. https://doi.org/10.1038/35084005.

Majeed, W., Magnuson, M., Hasenkamp, W., Schwarb, H., Schumacher, E.H., Barsalou, L., Keilholz, S.D., 2011. Spatiotemporal dynamics of low frequency BOLD fluctuations in rats and humans. Neuroimage 54, 1140–1150. https://doi.org/10.1016/j.neuroimage.2010.08.030.

Medaglia, J.D., Satterthwaite, T.D., Kelkar, A., Ciric, R., Moore, T.M., Ruparel, K., Gur, R.C., Gur, R.E., Bassett, D.S., 2018. Brain state expression and transitions are related to complex executive cognition in normative neurodevelopment. Neuroimage 166, 293–306. https://doi.org/10.1016/j.neuroimage.2017.10.048.

Nair, A., Treiber, J.M., Shukla, D.K., Shih, P., Müller, R.A., 2013. Impaired thalamocortical connectivity in autism spectrum disorder: a study of functional and anatomical connectivity. Brain 136, 1942–1955. https://doi.org/10.1093/brain/awt079.

Nickerson, L.D., Smith, S.M., Öngür, D., Beckmann, C.F., 2017. Using dual regression to investigate network shape and amplitude in functional connectivity analyses. Front. Neurosci. 11, 115. https://doi.org/10.3389/fnins.2017.00115.

Patriquin, M.A., DeRamus, T., Libero, L.E., Laird, A., Kana, R.K., 2016. Neuroanatomical and neurofunctional markers of social cognition in autism spectrum disorder. Hum. Brain Mapp. 37, 3957–3978. https://doi.org/10.1002/hbm.23288.

Power, J.D., Barnes, K.A., Snyder, A.Z., Schlaggar, B.L., Petersen, S.E., 2012. Spurious but systematic correlations in functional connectivity MRI networks arise from subject motion. Neuroimage 59, 2142–2154. https://doi.org/10.1016/j.neuroimage.2011.10.018.

Raichle, M.E., MacLeod, A.M., Snyder, A.Z., Powers, W.J., Gusnard, D.A., Shulman, G.L., 2001. A default mode of brain function. Proc. Natl. Acad. Sci. U.S.A. 98, 676–682. https://doi.org/10.1073/pnas.98.2.676.

Shmuel, A., Augath, M., Oeltermann, A., Logothetis, N.K., 2006. Negative functional MRI response correlates with decreases in neuronal activity in monkey visual area V1. Nat. Neurosci. 9, 569–577. https://doi.org/10.1038/nn1675.

Smith, S.M., Fox, P.T., Miller, K.L., Glahn, D.C., Fox, P.M., Mackay, C.E., Filippini, N., Watkins, K.E., Toro, R., Laird, A.R., Beckmann, C.F., 2009. Correspondence of the brain's functional architecture during activation and rest. Proc. Natl. Acad. Sci. U.S.A. 106, 13040–13045. https://doi.org/10.1073/pnas.0905267106.

Storey, J.D., Tibshirani, R., 2003. Statistical significance for genomewide studies. Proc. Natl. Acad. Sci. U.S.A. 100, 9440–9445. https://doi.org/10.1073/pnas.1530509100.

Takeda, Y., Hiroe, N., Yamashita, O., Sato, M., 2016. Estimating repetitive spatiotemporal patterns from resting-state brain activity data. Neuroimage 133, 251–265. https://doi.org/10.1016/j.neuroimage.2016.03.014.

Tong, Y., Hocke, L.M., Fan, X., Janes, A.C., Frederick, B.deB., 2015. Can apparent resting state connectivity arise from systemic fluctuations? Front. Hum. Neurosci. 9, 285. https://doi.org/10.3389/fnhum.2015.00285.

Tong, Y., Hocke, L.M., Licata, S.C., Frederick, B.deB., 2012. Low-frequency oscillations measured in the periphery with near-infrared spectroscopy are strongly correlated with blood oxygen level-dependent functional magnetic resonance imaging signals. J. Biomed. Opt. 17, 106004. https://doi.org/10.1117/1.JBO.17.10.106004.

Uddin, L.Q., Supekar, K., Menon, V., 2013. Reconceptualizing functional brain connectivity in autism from a developmental perspective. Front. Hum. Neurosci. 7, 458. https://doi.org/10.3389/fnhum.2013.00458.

Wang, W., Liu, J., Shi, S., Liu, T., Ma, L., Ma, X., Tian, J., Gong, Q., Wang, M., 2018. Altered resting-state functional activity in patients with autism spectrum disorder: a quantitative meta-analysis. Front. Neurol. 9, 556. https://doi.org/10.3389/fneur.2018.00556.

Wilson, M.A., McNaughton, B.L., 1994. Reactivation of hippocampal ensemble memories during sleep. Science 265, 676–679.

Xie, H., Zheng, C.Y., Handwerker, D.A., Bandettini, P.A., Calhoun, V.D., Mitra, S., Gonzalez-Castillo, J., 2019. Efficacy of different dynamic functional connectivity methods to capture cognitively relevant information. Neuroimage 188, 502–514. https://doi.org/10.1016/j.neuroimage.2018.12.037.

Yahata, N., Morimoto, J., Hashimoto, R., Lisi, G., Shibata, K., Kawakubo, Y., Kuwabara, H., Kuroda, M., Yamada, T., Megumi, F., Imamizu, H., Náñez, J.E.Sr, Takahashi, H., Okamoto, Y., Kasai, K., Kato, N., Sasaki, Y., Watanabe, T., Kawato, M., 2016. A small number of abnormal brain connections predicts adult autism spectrum disorder. Nat. Commun. 7, 11254. https://doi.org/10.1038/ncomms11254.

Yamashita, A., Yahata, N., Itahashi, T., Lisi, G., Yamada, T., Ichikawa, N., Takamura, M., Yoshihara, Y., Kunimatsu, A., Okada, N., Yamagata, H., Matsuo, K., Hashimoto, R., Okada, G., Sakai, Y., Morimoto, J., Narumoto, J., Shimada, Y., Kasai, K., Kato, N., Takahashi, H., Okamoto, Y., Tanaka, S.C., Kawato, M., Yamashita, O., Imamizu, H., 2019. Harmonization of resting-state functional MRI data across multiple imaging sites via the separation of site differences into sampling bias and measurement bias. PLoS Biol. 17, e3000042. https://doi.org/10.1371/journal.pbio.3000042.